Diabatic Quasi-Geostrophic Surface Frontogenesis

PETER R. BANNON

Department of the Geophysical Sciences, The University of Chicago, Chicago, IL 60637

MANKIN MAK[1]

National Center for Atmospheric Research,[2] Boulder, CO 80307

(Manuscript received 29 February 1984, in final form 4 June 1984)

ABSTRACT

Diabatic processes are included in a quasi-geostrophic model of surface frontogenesis due to an imposed horizontal deformation field. Analytic solutions are found for prescribed heating and for conditional instability of the second kind (CISK) parameterizations of cumulus convection.

The solutions for prescribed heating show that condensational heating has no direct effect on the surface potential temperature field. Indirectly this heating aloft may alter the surface frontogenesis by its induced ageostrophic horizontal divergences, but such an effect is estimated to be small. Condensational heating does, however, increase the strength of the mid-tropospheric frontogenesis and intensifies the vertical velocity above the surface front.

In contrast, prescribed boundary layer heating (e.g., surface heat transfer, subcloud evaporative cooling) modifies the surface temperature field directly and can also create a strong ageostrophic convergence near the ground.

Solutions for CISK heating parameterizations indicate that the heating and hence the ascending motion becomes concentrated in a narrow region on the warm side of the surface front. The dynamically induced heating is greater in magnitude and narrower in halfwidth for wave-CISK than for a CISK scheme proposed by Mak. An intermediate scheme which has features of both parameterizations is also studied.

1. Introduction

Recent theoretical studies of frontogenesis have emphasized dynamical aspects of frontal formation and structure and have been summarized by Hoskins (1982). Thermodynamic processes such as latent heat release, evaporative cooling of downdrafts and surface heat transfers are generally believed to be of secondary importance. For example, fronts have been observed in the ocean (Roden, 1975) and simulated in the laboratory (Fultz, 1952; Faller, 1956) where such processes are either small or nonexistent. Their presence, however, will modify the evolution and structure of the front. This paper explores some consequences of diabatic processes on frontogenesis.

Previous researchers have also addressed this problem. Sawyer (1956) and Eliassen (1959) show (numerically and analytically, respectively) that condensational heating will intensify the vertical circulation across a front. Their diagnostic models include the effects of heating by a reduction of the static stability in the region of rising motion (Sawyer) and by a prescribed elliptical region of heating (Eliassen). Hoskins and Bretherton (1972) prescribe the latent heat release in a semigeostrophic model of frontogenesis and find that weak heating strengthens frontogenesis and produces larger vertical velocities. However, details of the analysis are not presented. Hoskins (1974) includes latent heat release proportional to the vertical divergence at low levels in a two-dimensional numerical model with a frictional boundary layer. Again the field of rising motion is intensified but the model front is only slightly modified with a reduction of the surface longfront wind.

Ross and Orlanski (1978) include large-scale condensation and a nonlinear eddy viscosity formulation of cumulus convection in a two-dimensional numerical model of a cold front. For sufficiently strong deep cumulus convection, the cross-front circulation is overwhelmed by that of the convection: a convective system develops ahead of the front and propagates into the warm air faster than the front. Ross and Orlanski also address surface heating effects and its ability to help erode low-level capping inversions.

In contrast Williams, Chou and Cornelius (1981) include large-scale condensation and a convective adjustment parameterization in a time-dependent, two-dimensional numerical model. In the steady-state solutions, the latent heat release, which is predomi-

[1] Permanent affiliation: The University of Illinois, Urbana, IL 61801.

[2] The National Center for Atmospheric Research is sponsored by the National Science Foundation.

nately due to large-scale precipitation rather than cumulus convection, strengthens the front aloft but not at the surface. This heating also intensifies the vertical circulation with the strongest vertical motion in the mid-troposphere above the surface front.

The present investigation examines the effects of diabatic processes in a quasi-geostrophic framework. Analytic solutions for the response to heating are obtained here for the two-dimensional frontal model of Bannon (1983). Section 2 discusses the modification of this stretching deformation model of frontogenesis to include diabatic processes. Section 3 provides the Green's function solution to forcing incorporated into the lower boundary condition and into the potential vorticity equation. Section 4a uses these solutions to build a simple model with prescribed condensational heating. The results are consistent with those in Williams *et al.* (1981) but provide additional physical insight. Section 4b contrasts these solutions with ones for boundary layer heating (e.g., radiative and turbulent heat transfer, subcloud evaporative cooling).

Section 5 presents analytic solutions for different CISK parameterizations of cumulus convection. Here the heating is not prescribed but dynamically coupled to the dry surface front model. Charney and Eliassen (1964) and Ooyama (1964) originally proposed CISK to explain the formation of hurricanes. Subsequent investigators applied the concept to equatorial waves (e.g., Hayashi, 1970; Lindzen, 1974) and more recently to midlatitude convective systems (Raymond, 1975, 1976, 1983; Emanuel, 1982). Here we incorporate CISK into a prognostic quasi-geostrophic frontal model. In contrast, the recent work of Thorpe (1984) treats a CISK parameterization in a diagnostic quasi-geostrophic frontal model. As the dynamics are assumed to be inviscid and no moisture budget is included, Ekman-CISK and moisture partition (Kuo, 1974) schemes are precluded. Further, since the adjustment is instantaneous in quasi-geostrophic theory, CISK schemes with phase lags (Davies, 1979) are not considered. Instead a traditional wave-CISK approach is employed here and also a scheme proposed by Mak (1982, 1983). Because of the assumed vertical heating distribution, the two schemes can be formulated in a similar manner. Section 5 compares the two and also presents an intermediate scheme that has features of both. Section 6 summarizes the results.

2. The model

The quasi-geostrophic formulation is identical to that in Bannon (1983) with diabatic processes included. The geostrophic streamfunction ψ has the form

$$\psi(x, y, z, t) = \alpha xy + \phi(x, z, t), \tag{2.1}$$

where $\alpha > 0$ is the strength of the imposed Bergeron deformation field that drives the frontogenesis. Then the quasi-geostrophic potential vorticity equation for a Boussinesq fluid on an f-plane reduces to

$$\frac{d}{dt}\left(\frac{\partial^2\phi}{\partial x^2} + \frac{1}{S}\frac{\partial^2\phi}{\partial z^2}\right) = \frac{1}{S}\frac{\partial Q}{\partial z}, \tag{2.2}$$

where

$$\frac{d}{dt} \equiv \frac{\partial}{\partial t} - \alpha x \frac{\partial}{\partial x},$$

is the advection by the imposed deformation and the stratification parameter S is assumed constant. Here Q is the nondimensional heating function. Unless otherwise specified, the notation follows that of Pedlosky (1979) with the subscripts dropped.

The other flow variables are defined in terms of ψ as follows:

$$u = -\frac{\partial\psi}{\partial y}, \quad v = +\frac{\partial\psi}{\partial x}, \quad p = \psi, \tag{2.3a,b,c}$$

$$\theta = \frac{\partial\psi}{\partial z}, \quad w = \frac{1}{S}\left(Q - \frac{d\theta}{dt}\right). \tag{2.4a,b}$$

Here θ is the nondimensional deviation of the potential temperature from a stably stratified basic state θ_S, and (2.4b) is the quasi-geostrophic formulation of the first law of thermodynamics including diabatic processes.

Solutions to the governing equation (2.2) are sought subject to the condition that θ is bounded as $z \to \infty$ and $|x| \to \infty$. The kinematic lower boundary condition that $w = 0$ at $z = 0$ results in a heat equation of the form

$$\frac{d\theta}{dt} = Q \quad \text{at} \quad z = 0. \tag{2.5}$$

Unlike Bannon (1983), no orography is present and the lower boundary is flat. Specification of the initial streamfunction and of $Q(x, z, t)$ closes the problem.

In this paper the heating function Q is usually taken to be a prescribed function independent of the flow. As (2.2) and (2.5) are then linear equations, ϕ can be partitioned into an adiabatic (denoted by a subscript A) and a diabatic component (with subscript D):

$$\phi = \phi_A + \phi_D. \tag{2.6}$$

Here ϕ_A satisfies the homogeneous form of (2.2) and (2.5) and hence is identical to the solutions given in Bannon (1983) without orography; ϕ_D is the flow response to the heating function Q and satisfies (2.2) and (2.5). We assume that ϕ_A satisfies the inhomogeneous initial condition; therefore $\phi_D = 0$ at $t = 0$. Solutions for ϕ_D to prescribed heating are discussed in Sections 3 and 4.

The prescription of the heating function Q allows the basic physics of the diabatic effects on frontogenesis to be ascertained. A more realistic approach, perhaps,

would be a CISK-type parameterization in which the heating is a function of the flow. It is now shown, however, that a CISK-type solution can be expressed in terms of ϕ_D.

In a wave-CISK approach, the heating Q due to low-level moisture convergence is expressed as a function of the vertical velocity and hence by (2.4b) as a function of ϕ. Specifically, let the heating be a small linear function of ϕ,

$$Q = Q(\phi) = \Delta L(\phi), \tag{2.7}$$

where $|\Delta L| < 1$ is a measure of the smallness of the heating and L is a linear operator. Motivation for restricting attention to small values of Δ is based on the experience (see Introduction) that condensational heating only slightly modifies the frontogenesis in atmospheres with weak conditional instability. Moreover, a precipitation rate of 3 cm day^{-1} corresponds to a value of $|\Delta L|$ equal to unity if the heating is distributed uniformly over an 8 km depth of the atmosphere. It is shown *a posteriori* that the present approach is convergent for $\Delta \leqslant 1$.

Assume a perturbation series solution expansion for ϕ in terms of the parameter Δ

$$\phi = \phi_0 + \Delta\phi_1 + \cdots \Delta^n\phi_n \cdots. \tag{2.8}$$

The substitution of (2.7) and (2.8) into (2.2) and (2.5) yields to lowest order [$O(\Delta^0 = 1)$],

$$\frac{d}{dt}\left(\frac{\partial^2\phi_0}{\partial x^2} + \frac{1}{S}\frac{\partial^2\phi_0}{\partial z^2}\right) = 0, \tag{2.9}$$

$$\frac{d}{dt}\left(\frac{\partial\phi_0}{\partial z}\right) = 0 \quad \text{at} \quad z = 0. \tag{2.10}$$

This set is identical to that for the adiabatic flow component ϕ_A. Thus $\phi_0 = \phi_A$.

The order Δ^n set is

$$\frac{d}{dt}\left(\frac{\partial^2\phi_n}{\partial x^2} + \frac{1}{S}\frac{\partial^2\phi_n}{\partial z^2}\right) = \frac{1}{S}\frac{\partial}{\partial z}L(\phi_{n-1}), \tag{2.11}$$

$$\frac{d}{dt}\left(\frac{\partial\phi_n}{\partial z}\right) = L(\phi_{n-1}) \quad \text{at} \quad z = 0. \tag{2.12}$$

This latter set indicates that the nth term in the series (2.8) is forced by heating due to the known $(n-1)$th term and is identical in form to that for ϕ_D with prescribed heating. Analytic solutions with CISK heating are obtained using this approach and presented in Section 5. It is shown in Appendix A that this series approach corresponds to a Neumann series solution of the corresponding integral equation problem for the specific CISK parameterizations used here.

3. Green's function solution

a. *Exterior forcing*

In the absence of forcing in the interior ($z > 0$), the diabatic flow field ϕ satisfies

$$\frac{d}{dt}\left(\frac{\partial^2\phi_E}{\partial x^2} + \frac{1}{S}\frac{\partial^2\phi_E}{\partial z^2}\right) = 0, \tag{3.1}$$

subject to the initial condition that $\phi_E = 0$ at $t = 0$ and to the lower boundary condition

$$\frac{d}{dt}\left(\frac{\partial\phi_E}{\partial z}\right) = Q(x, t) = \delta(t - t_0)\delta(x - x_0) \quad \text{at} \quad z = 0, \tag{3.2}$$

where δ is the Dirac delta function. Physically $Q(z = 0)$ represents the net effect of radiative and turbulent heat transfer processes at the surface. Here a subscript E denotes the Green's function solution to this surface or exterior forcing.

The solution of (3.1) in terms of the potential temperature has been shown by Bannon [1983, see (2.19)] to be

$$\theta_E(x, z, t) = \int_{-\infty}^{+\infty} A_E(k, t)e^{ikx}e^{\sqrt{Sk^2}z}dk, \tag{3.3}$$

using Fourier transform techniques.

The solution to (3.2) with this heating distribution can be found by standard Green's function techniques to be

$$\left.\frac{\partial\phi_E}{\partial z}\right|_{z=0} = \theta_E(x, 0, t) = H(t - t_0)\delta[xe^{\alpha(t-t_0)} - x_0], \tag{3.4}$$

where H is the Heaviside step function. The form of this solution indicates that θ_E is zero before the heating ($t < t_0$). After the heating ($t > t_0$), the warm anomaly is advected towards the dilatation axis ($x = 0$).

$A_E(k, t)$ is found by equating (3.3) at $z = 0$ with (3.4) to obtain

$$A_E(k, t) = \frac{H(t - t_0)e^{\alpha(t-t_0)}}{2\pi}\exp[-ikx_0e^{\alpha(t-t_0)}]. \tag{3.5}$$

Substituting this expression into (3.3) and evaluating the integral, we obtain

$$\theta_E(x, z, t) = \frac{H(t - t_0)e^{\alpha t_0}}{\pi}\frac{Z}{(X - X_0)^2 + Z^2}, \tag{3.6}$$

where $X = x\exp(\alpha t)$, $X_0 = x_0\exp(\alpha t_0)$ and $Z = \sqrt{S}z \times \exp(\alpha t)$. The structure of (3.6) is similar to that of the occluded front of Bannon (1983). Here the occlusion is infinite at the surface ($z = 0$) and is being advected towards the dilatation axis.

By the properties of a Green's function, the solution for a general exterior heating of the form $Q(x, t)$ is

$$\theta_D(x, z, t) = \int_0^{\infty} dt_0 \int_{-\infty}^{+\infty} dx_0\theta_E(x, z, t)Q(x_0, t_0), \tag{3.7}$$

where θ_E is defined by (3.6).

b. Interior forcing

In this section the response is determined to a point source forcing in the interior ($z > 0$). Specifically (2.2) is

$$\frac{d}{dt}\left(\frac{\partial^2\phi_I}{\partial x^2} + \frac{1}{S}\frac{\partial^2\phi_I}{\partial z^2}\right) = \delta(t - t_0)\delta(x - x_0)\delta(z - z_0), \tag{3.8}$$

where the subscript I denotes the Green's function response to forcing in the interior and the lower boundary condition is

$$\frac{d}{dt}\left(\frac{\partial\phi_I}{\partial z}\right) = 0 \quad \text{at} \quad z = 0. \tag{3.9}$$

As ϕ_I is initially zero everywhere and no forcing is present at the surface, the boundary condition (3.9) may be replaced by

$$\frac{\partial\phi_I}{\partial z} = 0 \quad \text{at} \quad z = 0. \tag{3.10}$$

Recall that it is assumed that the adiabatic solution incorporates the inhomogeneous lower boundary condition.

A solution to (3.8) can be found using the results of the previous subsection. Comparing (3.2), where the solution is (3.4), with (3.8), one finds

$$\frac{\partial^2\phi_I}{\partial x^2} + \frac{1}{S}\frac{\partial^2\phi_I}{\partial z^2} = \bar{e}^{\alpha(t-t_0)}H(t - t_0)\delta[x - x_0\bar{e}^{\alpha(t-t_0)}]\delta(z - z_0), \tag{3.11}$$

using properties of the δ-function. The solution to the elliptic Green's function problem of (3.11) is well-known in mathematical physics. The solution is

$$\phi_I = \frac{\sqrt{S}}{4\pi}\bar{e}^{\alpha(t-t_0)}H(t - t_0)[\ln R_+ + \ln R_- - 4\alpha t], \tag{3.12}$$

where $R_\pm = (X - X_0)^2 + Z_\pm^2$, $Z_\pm = \sqrt{S}(z \pm z_0) \times \exp(\alpha t)$ and X and X_0 are defined following (3.6). In obtaining (3.12), the method of images has been used to satisfy the boundary condition (3.10).

The corresponding potential temperature field is

$$\theta_I(x, z, t) = \frac{S}{2\pi}e^{\alpha t_0}H(t - t_0)\left(\frac{Z_+}{R_+} + \frac{Z_-}{R_-}\right). \tag{3.13}$$

Before the forcing ($t < t_0$), $\theta_I = 0$. After the forcing ($t > t_0$), the thermal anomaly is advected to the dilatation axis. Unlike the solution for surface forcing, (3.6), θ_I vanishes at the surface and decays to zero as $t \to \infty$, [θ_E at ($z = 0$, $x = x_0$) remains nonzero as $t \to \infty$.] The latter behavior is consistent with that of the inhomogeneous component [θ_I in (2.17)–(2.18)] of Bannon (1983).

The solution to a general heating function $Q(x, z, t)$ in the interior is

$$\theta_D(x, z, t) = \frac{1}{S}\int_0^\infty dt_0 \int_{-\infty}^{\infty} dx_0 \int_0^\infty dz_0 \times \theta_I(x, z, t)\frac{\partial Q}{\partial z_0}(x_0, z_0, t_0), \tag{3.14}$$

where Q is the prescribed heating and θ_I is defined by (3.13).

4. Simple models with prescribed heating

a. Condensational heating

As a simple representation of latent heat release, the heating is taken to be

$$Q(x, z, t) = \frac{F(t)[H(z - z_B) - H(z - z_T)]}{[1 + (x - b)^2/a^2]}, \tag{4.1}$$

where F is its time dependence and again H is the Heaviside step function. In the vertical the heating is uniform within the region $z_B < z < z_T$ and zero elsewhere. Horizontally the heating is a maximum at $x = b$ and decays laterally with a halfwidth a. For definiteness the geometric parameters are set to be $b = -0.5$, $a = 0.25$, $z_B = 0.20$, $z_T = 1$. Since $z_B > 0$, $Q(x, 0, t) = 0$ and there is no surface forcing. For reference the spatial structure of (4.1) is plotted in Fig. 1. In this and subsequent figures, the characteristic length and height of the flow is assumed to be 1000 and 10 km, respectively.

The solution to the heating (4.1) is found upon substituting into (3.14). The integral in z_0 is trivial; that in x_0 can be evaluated analytically by convolution using Fourier transforms. The result is

$$\theta_D = \frac{a}{2}\sum_{i=1}^{4} d_i \operatorname{sgn}(Z_i)\int_0^t dt_0 \frac{e^{\alpha t_0}F(t_0)A_i}{(A_i^2 + B^2)}, \tag{4.2}$$

where sgn denotes the sign function with sgn(0) = 0, $A_i = a\exp(\alpha t_0) + |Z_i|$, $d_i = +1, +1, -1, -1$; $Z_i = \sqrt{S}(z - z_i)\exp(\alpha t)$ with $z_i = z_B, -z_B, z_T, -z_T$ and $B = x\exp(\alpha t) - b\exp(\alpha t_0)$.

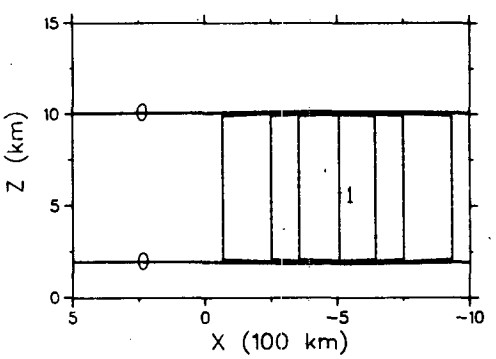

FIG. 1. Spatial distribution of the prescribed condensational heating (4.1). The nondimensional contour interval (C.I.) is 0.25.

Figure 2 displays the time evolution of θ_D given by (4.2) with $S = 1$ for an instantaneous heating given by $F(t) = \delta(t)$ where δ is the Dirac delta function. The notation $t = +0$ denotes the time just after the heating. Comparison of Figs. 1 and 2a indicates that the structure of the thermal anomaly is not identical to the heating distribution. Laterally the anomaly is broader than the heating and vertically it is not confined to the region of heating, $z_B < z < z_T$. In addition there are regions of negative anomaly both directly above and below the region of heating. This response results from the adiabatic warming and cooling associated with the induced vertical velocity field. In general, the heating has increased (decreased) the lower (upper) level static stability.

For $t > +0$, the θ_D field is advected towards the dilatation axis while decaying in amplitude (see Fig. 2b). This behavior arises from the action of the imposed deformation field. Eventually $\theta_D \rightarrow 0$ as $t \rightarrow \infty$.

It is important to note that the surface temperature field is unaffected by the interior heating. Here $\theta_D(x, 0, t)$ is identically zero. This result reflects the boundary condition (3.10). Aloft, however, the heating tends to increase the strength of the front (assuming the heating occurs in the warm sector).

The vertical velocity can be found from (4.2) using the heat equation (2.4b). The result is

$$w = \frac{Q}{S} - \frac{a}{2S}\sum_{i=1}^{4} d_i\left\{\mathrm{sgn}(Z_i)\frac{e^{\alpha t}F(t)A_i}{(A_i^2 + B^2)}\bigg|_{t_0=t} + \int_0^{\alpha t} d(\alpha t_0)e^{\alpha t_0}F(t_0)Z_i(B^2 - A_i^2)/(A_i^2 + B^2)^2\right\}. \quad (4.3)$$

The associated ageostrophic horizontal divergence field is, from continuity,

$$\frac{\partial u_a}{\partial x} = -\frac{1}{S}\frac{\partial Q}{\partial z} + \frac{ae^{\alpha t}}{2\sqrt{S}}\sum_{i=1}^{4} d_i\left\{e^{\alpha t}\frac{F(t)(B^2 - A_i^2)}{(A_i^2 + B^2)^2}\bigg|_{t_0=t} + \int_0^{\alpha t_0} d(\alpha t_0)e^{\alpha t_0}F(t_0)\left[\frac{B^4 - A_i^4 - 2|Z_i|A_i}{(A_i^2 + B^2)^3} \times (3B^2 - A_i^2)\right]\right\}, \quad (4.4)$$

where the subscript a denotes an ageostrophic quantity. Despite the presence of a vertically discontinuous heating profile, both the vertical velocity and its vertical gradient are continuous.

These fields are displayed for the instantaneous heating in Fig. 3 at $\alpha t = 1$ for $S = \alpha = 1$. As with the potential temperature, these fields are decaying as they move towards the dilatation axis. Fig. 3a displays an essentially direct circulation with maximum rising motion in the region of heated fluid. Above and below this region there is subsidence. Laterally, the weak broadscale sinking compensates the strong rising motion. As Fig. 3b indicates, this pattern of vertical velocity has large ageostrophic divergence (convergence) at $z = 1.0$ (0.2). In comparison the ageostrophic divergence is relatively weak at the surface.

The net effect of a sustained condensational heating on these fields is depicted in Fig. 4. Here the heating rate is assumed constant in time [$F(t) = C$], crudely modeling the four day integration of Williams *et al.* (1981), which reaches a steady state. The fields are evaluated from (4.2–4.4) with $\alpha t = 2$ by numerical Gaussian quadrature. The nondimensional heating rate C is set to ½ here so that the time integrated heating is identical to the δ-function case of Figs. 2 and 3. The imposed deformation field displaces the maximum response toward the dilatation axis. Comparison of Fig. 4a with Fig. 2 of Williams *et al.* (1981) indicates qualitative agreement: there is warming in the middle troposphere and cooling aloft. For warm sector precipitation, this warming distribution intensifies the front at midlevels. The displacement of the thermal response towards the dilatation axis also appears in their results, comparing their Figs. 2d and

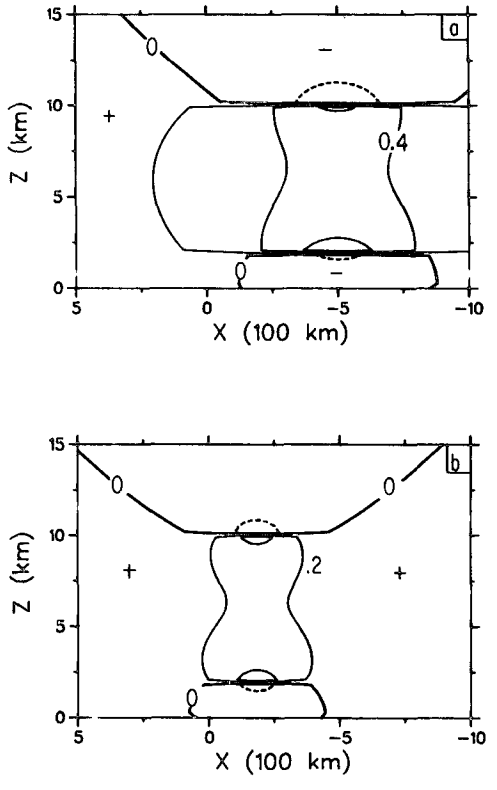

FIG. 2. Time evolution of the nondimensional potential temperature (4.2) for an instantaneous δ-function condensational heating at $t = 0$ with the spatial structure depicted in Fig. 1. The top panel is for time $\alpha t = +0$; the bottom for $\alpha t = 1$. C.I. = 0.20. In this and subsequent figures the heavy solid line is the zero contour, negative contours are dashed and positive and negative regions are indicated by plus (+) and minus (−), respectively.

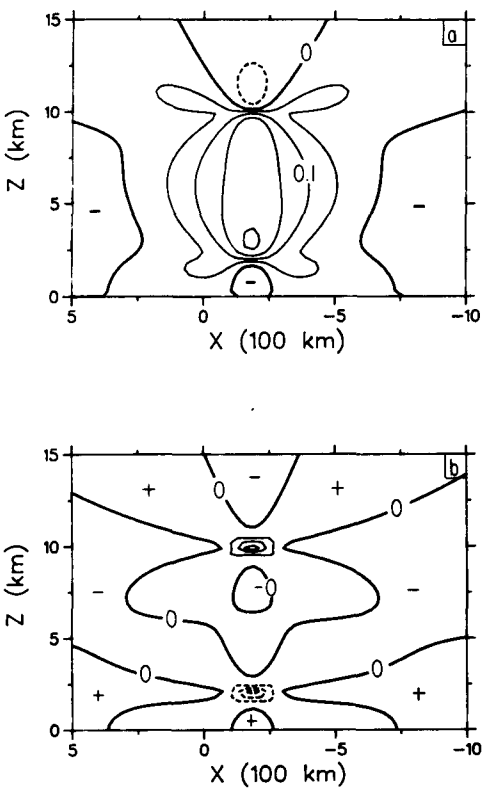

FIG. 3. The nondimensional vertical velocity (top, C.I. = 0.05) and ageostrophic horizontal divergence (bottom, C.I. = 1.0) at the time $\alpha t = 1$ associated with the instantaneous condensational heating case of Fig. 2.

7. The stronger vertical velocities at midlevels and the elongation of the region of rising motion toward the dilatation axis are also consistent in the two studies (see our Fig. 4b and their Figs. 5d and 7).

The ageostrophic horizontal divergence displayed in Fig. 4c shows extrema at $z = 0.2$ and 1.0 associated with the step function nature of the heating (4.1). The frontogenetic convergence along $z = z_B$ has two maxima, a weak broad maximum near the region of greatest heating ($x = b$) and a smaller but stronger one near the dilatation axis ($x = 0$). The latter is induced by the large-scale deformation acting on the thermal anomaly generated by the heating at earlier times. A similar pattern holds aloft along $z = z_T$ for the ageostrophic frontolytic divergence. Between these two levels the divergence field is weak.

Figure 5 summarizes the sensitivity of the surface ageostrophic horizontal convergence $(-\partial u_a/\partial x)$ with plots for various parameter settings. Fig. 5a shows the effects of the time t and stratification S on $(-\partial u_a/\partial x)$. It is seen that the surface convergence is only slightly enhanced if t (or α) is doubled. [Inspection of (4.3) indicates that for $F(t) = C$ the convergence is a function of αt only.] Thus the fields of Fig. 4 represent approximate steady-state results. A reduction of the stratification parameter S results in a stronger convergence associated with a more intense vertical circulation. Fig. 5b investigates the effects of the heating geometry. In each curve the total condensational heating is the same. The surface convergence is intensified if the cloud is lowered, thinned, narrowed or displaced towards the dilatation axis.

In comparison, the surface convergence associated with adiabatic frontal development like $\theta(x, 0, t) = -2/\pi \tan^{-1}[x \exp(\alpha t)]$ is, [Bannon, 1983; (3.11)],

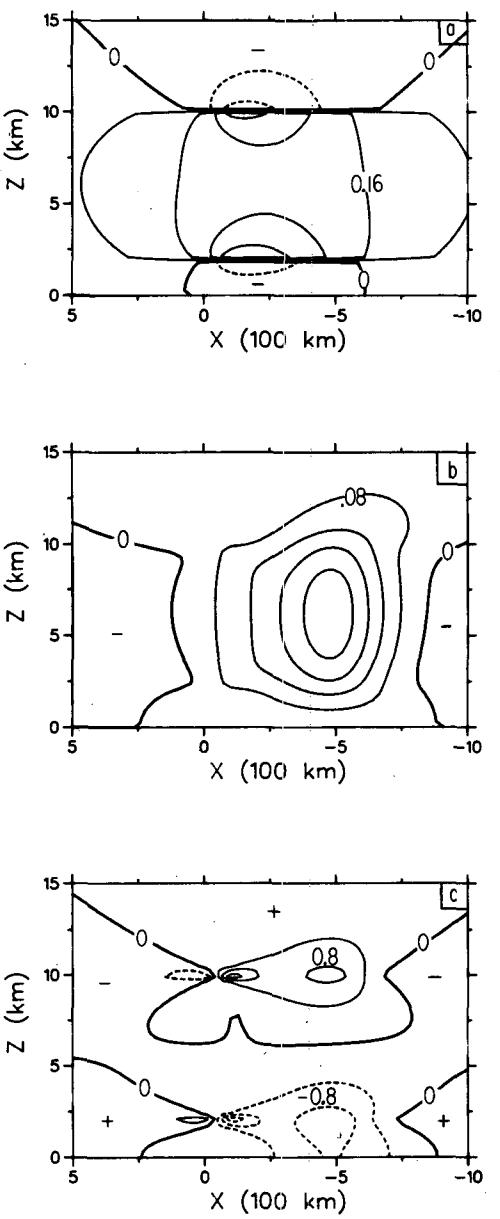

FIG. 4. The nondimensional potential temperature (top, C.I. = 0.08), vertical velocity (middle, C.I. = 0.08) and ageostrophic horizontal divergence (bottom, C.I. = 0.40) at the time $\alpha t = 2$ forced by a constant condensational heating of the form (4.1) with magnitude $F(t) = 0.5$.

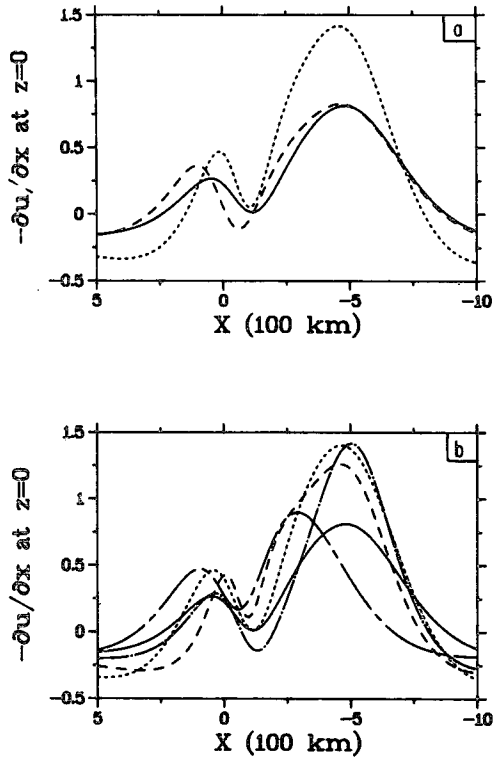

FIG. 5. Surface convergence ($-\partial u_a/\partial x$ at $z = 0$) due to constant condensational heating (4.1) as a function of x. The solid line in each panel is the case depicted in Fig. 4 ($\alpha t = 2$ and $S = 1$) and is the reference case. In (a), the dashed line has time t doubled; the dotted line has the stratification parameter S halved compared to the reference. In (b) the total heating is the same for each curve but its spatial distribution is altered. The dashed line has the cloud base lowered 1 km ($z_B = 0.1$), while the dotted line has the cloud top lowered to 6 km ($z_T = 0.6$) compared to the reference ($z_B = 0.2$, $z_T = 1.0$, $a = 0.25$, $b = -0.5$). The chain-dot case has the cloud width halved ($a = 0.125$); the chain-dash case has the cloud center displaced toward the dilatation axis ($b = -0.25$).

$$-\frac{\partial u_a}{\partial x} = -\frac{2}{\pi}\frac{\alpha}{\sqrt{S}}\frac{x(1+e^{2\alpha t})}{(1+x^2e^{2\alpha t})}, \qquad (4.5)$$

which has a maximum of $\alpha[\exp(\alpha t) + \exp(-\alpha t)]/(\pi\sqrt{S}) = 2.40$ at $x = -\exp(-\alpha t) = -0.135$ for $\alpha = S = 1$. This result suggests that the effect of the surface convergence induced by condensational heating is small compared to that of the frontogenesis.

The impact that the sustained interior heating ($F(t) = \frac{1}{2}$) has on the frontal structure is illustrated in Fig. 6 where the vertical velocity and dimensional (here denoted by a subscript asterisk) potential temperature θ_* is plotted for a frontal solution with and without the heating at the time $\alpha t = 2$. The potential temperature θ_* is given by

$$\theta_* = \theta_S(z_*)[1 + \epsilon\,\mathrm{Fr}(\theta_A + \theta_D)], \qquad (4.6)$$

where $\theta_S(z_*) = 273\ \mathrm{K} + (3\ \mathrm{K/km})z_*$ is the static potential temperature field, $\epsilon = 0.2$ the Rossby number and $\mathrm{Fr} = 0.1$ the Froude number. The adiabatic field θ_A is obtained from Bannon (1983) for an initial field $\theta_A(x, z, 0) = -(4/\pi)\tan^{-1}(x)$ and θ_D is given by (4.2). The front is unaffected by the heating directly at the surface. At cloud base ($z_B = 0.2$) the isentropes are flattened. In the cloud ($0.2 < z < 1.0$), they are lowered, while aloft ($z > 1.0$) they are raised. These features are evident in Figs. 2a and d of Williams *et al.* (1981). Just at cloud top, the unrealistic discontinuous heating used here has generated a region near $x = -0.25$ that is convectively unstable. Comparison of Figs. 6c and d indicates that the rising motion in the warm sector is $\sim$ doubled by the heating.

b. *Boundary layer heating*

Here the effects of heating located near the surface are ascertained for forcing of the form

$$Q(x, z, t) = \frac{F(t)[1 - H(z - z_B)]}{[1 + (x - b)^2/a^2]}. \qquad (4.7)$$

In this case $Q(x, 0, t) \neq 0$ and the solution is the sum of the response to surface and interior contributions. Substitution of (4.7) into (3.7) and (3.14) and evaluation of the integrals yield expressions for θ_D, w and $\partial u/\partial x$ that can be written in a form identical to (4.2)–(4.4) but now $z_i = 0, 0, z_B, -z_B$ and $\mathrm{sgn}(0) = 1$ for $i = 1$ and 2. Because of this relation between the solutions, the behavior of the response to (4.7) is generally similar to that for (4.1) and extensive display of results is not warranted.

A fundamental feature of the present results is that the heating (4.7) directly alters the surface potential temperature field and hence can modulate the surface front. Further, as shown below, the ageostrophic divergence field can significantly alter the frontogenesis. Neither of these two features of the boundary layer results is present in the case with condensational heating.

Application of the heating (4.7) or similar expressions is hampered by the lack of specific observational details of the mechanism, magnitude, and distribution of the boundary layer heating associated with fronts. In an attempt to gain insight into the impact of such heating, a crude model of one possible mechanism is discussed. Others (e.g., differential insolation due to cloud cover or surface thermal inhomogeneities) may also be important.

One mechanism is subcloud evaporative cooling of the rainshaft. Fujita (1959) estimates that the ratio of such evaporation to the surface rainfall is typically $\frac{3}{16}$ to $\frac{1}{4}$ ($\frac{1}{16}$ to $\frac{1}{8}$) for a thunderstorm (warm frontal rain) over land for a cloud base of about 2 km. To model this effect it is assumed that the cooling is uniform below cloud base with a lateral extent identical to the condensational heating. Then (4.7) represents this situation with $z_B = 0.2$, $b = -\frac{1}{2}$ and $a = 0.25$. If the cloud top is at $z_T = 1.0$, as in Section 4a, and there is steady rain with $F(t) = \frac{1}{2}$ in (4.1) (a

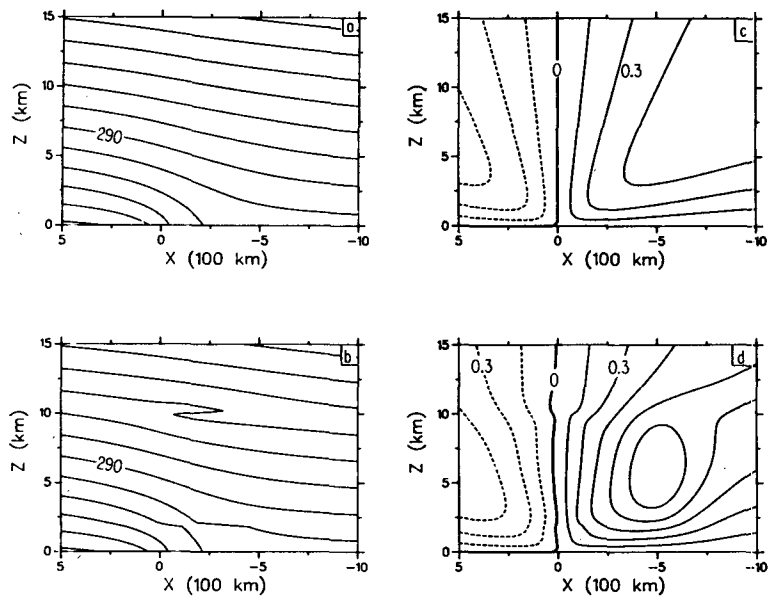

FIG. 6. Dimensional potential temperature (4.6) in K at $\alpha t = 2$ for a front without [Panel (a)] and with [Panel (b)] constant condensational heating [(4.1) with $F(t) = \frac{1}{2}$]. C.I. = 5 K. Panels (c) and (d) show the associated vertical velocity field without and with heating, respectively. C.I. = 0.15.

maximum rainfall of about 1.5 cm/day), then $F(t)$ in (4.7) should vary from $-\frac{1}{8}$ to $-\frac{1}{2}$ [since the mass of air cooled in (4.7) is one fourth of that warmed by (4.1)] for warm frontal rain through thundershowers.

Figure 7 displays the θ, w and $\partial u/\partial x$ fields at $\alpha t = 2$ for the forcing (4.7) with $F(t) = -\frac{1}{4}$, representing a dimensional cooling rate of 2.3 K day^{-1}. The nondimensional potential temperature field (Fig. 7a) exhibits strong cooling below cloud base with a surface maximum; there is weak warming aloft associated with the thermally direct circulation cell (Fig. 7b). This cooling is frontolytic (frontogenetic) in the case of pre-cold (-warm) frontal precipitation. In contrast with the condensational heating case (Fig. 4b) which has one maximum above cloud base, the vertical velocity has two minima below cloud base, a weak one near the region of maximum cooling at $x = -0.5$ and a stronger one closer to the dilatation axis $x = 0$. The latter is associated with the deformation of the surface thermal anomaly by the large-scale forcing. The ageostrophic horizontal divergence (Fig. 7c) associated with the vertical motion field is most intense at the surface, decays rapidly with height and reverses sign near cloud base $z = z_B$. This field is predominantly frontolytic (frontogenetic) for $x < 0$ (>0). The fields for the case of prescribed precipitation with subcloud evaporative cooling consist of the sum of Figs. 4 and 7 (not shown).

The relative strength of this ageostrophic flow is assessed in Fig. 8 which plots the surface convergence for the present case (dashed line), the condensational heating case (solid line) of Section 4a and the frontal case of (4.5) (heavy solid line). Inspection of this figure indicates that the ageostrophic surface divergence due to boundary layer heating can dominate that due to condensational heating (recall that the total heating of the former is a quarter of the latter). In addition, it is comparable in magnitude but opposite in sign to that associated with the frontogenesis. In the case of prescribed precipitation with subcloud evaporative cooling, the solid and dashed curves should be added together (not shown). In such a case, a significant frontolytic divergence results near the dilatation axis with cancellation elsewhere.

5. CISK parameterization of cumulus heating

In a CISK parameterization of cumulus heating, the heating Q is usually assumed proportional to the low-level moisture convergence. Here temporarily following standard wave-CISK theory, the heating is assumed proportional to the large-scale vertical velocity w_B just below cloud base at $z = z_B$,

$$Q(x, z, t) = \Delta S G(z) w_B(x, z_B, t), \qquad (5.1)$$

where the factor of S in (5.1) assures that Δ is an intrinsically nondimensional measure of the magnitude of the heating and is independent of the scaling. The vertical distribution of the heating is described by $G(z)$ and taken to be a known function of height. Physically it is required that there is no heating below cloud base

$$G(z < z_B) = 0. \qquad (5.2)$$

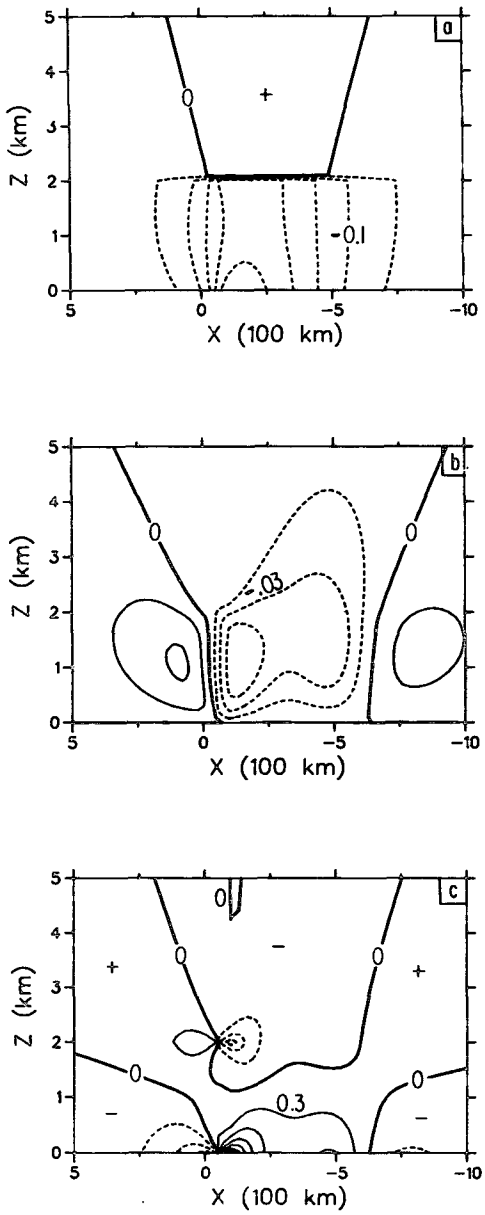

FIG. 7. The nondimensional potential temperature (top, C.I. = 0.05), vertical velocity (middle, C.I. = 0.015) and ageostrophic horizontal divergence (bottom, C.I. = 0.30) at the time $\alpha t = 2$ forced by a constant boundary layer heating of the form (4.7) with magnitude $F(t) = -0.5$.

The specific form of $G(z)$ used here is one of uniform heating within the cloud

$$G(z) = H(z - z_B) - H(z - z_T). \tag{5.3}$$

This form is motivated by the desire for simple analytic solutions. The parameterization is closed with an expression for w_B. From (2.4b) and (5.2) one finds just below cloud base

$$w_B(x, z_B, t) = -\frac{1}{S}\frac{d\theta}{dt}\bigg|_{z=z_B}, \tag{5.4}$$

and the heating does not explicitly appear in the expression for w_B. Hence the linear operator in (2.7) is

$$L(\phi) = -G(z)\left[\frac{d}{dt}\left(\frac{\partial\phi}{\partial z}\right)\right]_{z=z_B}. \tag{5.5}$$

Thus the potential temperature associated with the nth term in the expansion (2.8) is

$$\theta_n(x, z, t) = -\frac{1}{S}\int_0^\infty dt_0 \int_{-\infty}^{+\infty} dx_0 \int_0^\infty dz_0 \times \left[\theta_I(x, z, t)\frac{dG(z_0)}{dz_0}\frac{d}{dt}\theta_{n-1}(x_0, z_B, t_0)\right], \tag{5.6}$$

by substituting (5.1) and (5.4) into (3.14). Recall that θ_I is given by (3.13) and that θ_0 is θ_A, the adiabatic solution. For definiteness θ_A is taken to be the adiabatic frontal solution to an initial field $\theta(x, z, 0) = -4/\pi \times \tan^{-1}x$. Then θ_A is found from (3.3) of Bannon (1983) to be in the present notation,

$$\theta_A = \theta_0 = \frac{-4}{\pi}\left[\bar{e}^{2\alpha t}\tan^{-1}X + (1 - \bar{e}^{2\alpha t})\tan^{-1}\frac{X}{1+Z}\right]. \tag{5.7}$$

The triple integrals in (5.6) can be evaluated analytically with these choices of θ_A and $G(z)$. The procedure is given in Appendix B. The result is

$$\theta = \theta_0 + \Delta\theta_1 + \Delta^2\theta_2 + \cdots, \tag{5.8}$$

where the first contribution by the heating is

$$\theta_1 = -\frac{1}{\pi}(1 - \bar{e}^{2\alpha t})\sum_{m=1}^{8} a_m \operatorname{sgn}(z - b_m) \times \tan^{-1}\frac{X}{1 + \sqrt{S}e^{\alpha t}c_m}, \tag{5.9}$$

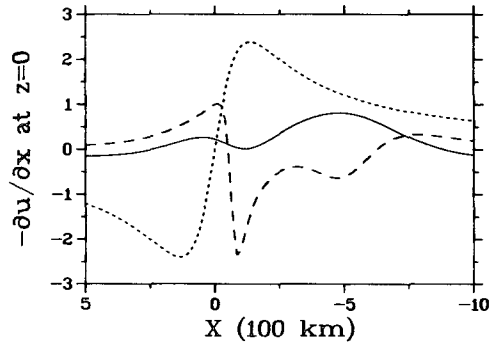

FIG. 8. Surface convergence ($-\partial u_a/\partial x$ at $z = 0$) at $\alpha t = 2$ as a function of x. The solid line is the constant condensational heating case of Fig. 4 associated with the forcing (4.1) with $F(t) = \frac{1}{2}$. The dashed line is the constant boundary layer heating case of Fig. 7 associated with the forcing (4.7) with $F(t) = -\frac{1}{4}$. The dotted line is the adiabatic frontal solution (4.5).

where $a_m = (-1)^m$ $m \leqslant 4$ and $a_m = (-1)^{m+1}$ $m \geqslant 5$, $b_m = z_B, z_B, -z_B, -z_B, z_T, z_T, -z_T, -z_T$ and $c_m = |z - b_m| + (1 - (-1)^m)z_B/2$. The second contribution is

$$\theta_2 = \frac{(1 - \bar{e}^{2\alpha t})}{2\pi} \sum_{m=1}^{8} a_m \operatorname{sgn}(z_B - b_m) \sum_{i=1}^{4} d_i \operatorname{sgn}(z - z_i) \times \tan^{-1}\left[\frac{X}{1 + \sqrt{S}e^{\alpha t}(c_{mB} + |z - z_i|)}\right], \quad (5.10)$$

where d_i and z_i are defined following (4.2) and c_{mB} is c_m evaluated at $z = z_B$. Higher order terms are found in a similar manner. The associated vertical velocity field is of the form

$$\left.\begin{aligned} w &= w_0 + \Delta w_1 + \Delta^2 w_2 + \cdots \\ w_0 &= w_A \end{aligned}\right\}, \quad (5.11)$$

where each term is determined from the corresponding θ-field using (2.4b).

The associated heating is expressed in terms of a similar series:

$$Q = \Delta S[Q_0 + \Delta Q_1 + \Delta^2 Q_2 + \cdots], \quad (5.12)$$

where

$$Q_k = G(z)w_k(x, z_B, t). \quad (5.13)$$

Here Q_0 is the cumulus heating assumed induced by the dry frontal dynamics $w_0 = w_A$. Together all the higher order terms represent the net heating induced by the response to Q_0. Individually, for $k \geqslant 1$, Q_k is the heating induced by the response to the forcing Q_{k-1}.

In accordance with wave-CISK theory, w_B is the vertical velocity just below cloud base. Mathematically this implies that $\operatorname{sgn}(z - z_B) = -1$ when $z = z_B$ in (5.9) and (5.10). As the vertical velocity field is continuous, then w_B is also the vertical motion field just above cloud base. In the cloud, however, there is heating and (5.4) should be replaced by

$$w_B(x, z_B, t) = -\frac{1}{S}\frac{d\theta}{dt}\bigg|_{z_B} + \frac{Q(x, z_B, t)}{S} \quad (5.14)$$

just above cloud base.

Recently, Mak (1982, 1983) has argued that the scale-selection shortcoming of wave-CISK arises due to the implicit use of (5.14) and suggested that the parameterization (5.1) with w_B be given by the adiabatic vertical velocity just above cloud base, namely,

$$w_B(x, z_B, t) = -\frac{1}{S}\frac{d\theta}{dt}\bigg|_{z_B}. \quad (5.15)$$

Mathematically one takes $\operatorname{sgn}(z - z_B) = +1$ when $z = z_B$ in this parameterization, referred to as the Mak scheme. An intermediate case, which is the average of wave-CISK and Mak schemes, suggests itself and is obtained by taking $\operatorname{sgn}(z - z_B) = 0$ when $z = z_B$.

Figure 9 plots the horizontal structure of Q_k, $k = 1$–5, for both wave-CISK and the Mak scheme. Here $\alpha = S = 1$ and $t = 2$. Each has odd symmetry about the origin and the region shown ($x \leqslant 0$) is assumed to correspond to a region of rising motion of the front ($w_A \geqslant 0$). For wave-CISK, each term Q_k is predominantly positive; higher order terms change sign and fluctuate about zero for large $|x|$. As k increases, the magnitude of the heating is reduced and its peak moves towards the origin. Each term acts to augment the net cumulus heating and shift the maximum heating toward the origin. The net response of the wave-CISK parameterization is shown in Fig. 10 and represents the sum of the curves in Fig. 9a plus Q_0. Compared to Q_0, the heating has been roughly doubled in magnitude and narrowed in halfwidth.

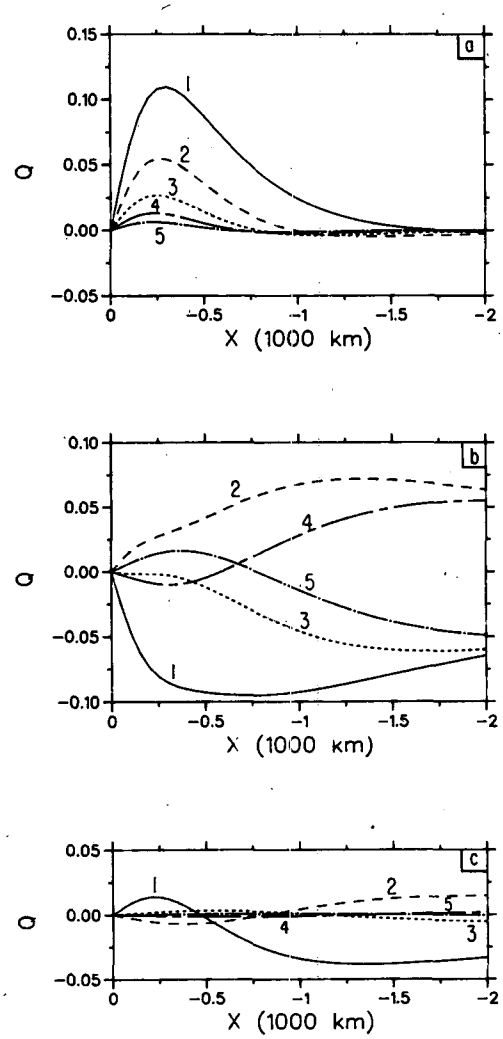

FIG. 9. The self-induced heating terms Q_k ($k = 1$–5) given by (5.13) as a function of x at $\alpha t = 2$. Panels (a), (b) and (c) refer to wave-CISK (WC), the Mak scheme (MC), and an intermediate (IC) cumulus parameterization.

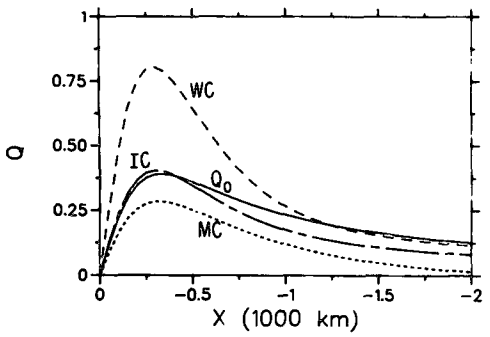

FIG. 10. The total self-induced heating Q given by (5.12) as a function of x at $\alpha t = 2$ with the heating parameter $\Delta = 1$. The labels WC, MC, and IC refer to the wave-CISK, Mak scheme and intermediate CISK parameterizations. Each curve represents the sum of the associated curves in Fig. 10 plus Q_0, where Q_0 is the heating in the absence of higher order feedbacks.

These results should be contrasted to those for the Mak scheme. Fig. 9b indicates that here the Q_k alternate sign and the absolute maximum of each term decreases and moves away from the origin as k increases. This scheme converges (for $\Delta \leqslant 1.0$) less rapidly than wave-CISK and the rate of convergence decreases as $|x|$ increases. Physically one may ascribe the regions of negative response to the fact that drying the net atmospheric column and warming and moistening the upper atmosphere causes a stabilizing influence of the cumulus clouds. The net effect of the wave-CISK parameterization is seen in Fig. 10. The heating has again been narrowed in halfwidth but now its magnitude has also been reduced.

The intermediate parameterization that combines the features of both the wave-CISK and Mak schemes is illustrated in Figs. 9c and 10. Here the initial adjustment of the cumulus field, Q_1, augments the heating close to the origin but suppresses it farther out. The higher order terms alternate sign and have absolute maxima that occur at larger value of $|x|$. The net effect is to increase the heating maximum, reduce its halfwidth and reduce its total.

Figure 11 presents contour plots of the dimensional θ field and the vertical velocity for the intermediate parameterization with $\Delta = 1$ at $\alpha t = 2$. The parameter settings are the same as that used in (4.6). The plotted fields include the adiabatic frontal solution plus the first three diabatic terms in the series (5.8) and (5.11). Comparison of these fields can be made with those in Fig. 6 for constant prescribed heating. The major differences occur on the cold air side ($x > 0$) of the front where the simple CISK parameterization (5.1) permits a net negative induced heating with an associated strong downdraft. The negative heating reduces (increases) the static stability at low (high) levels. The rising motion for the CISK heating is comparable in magnitude to that for the prescribed heating but it lies closer to the dilatation axis. This latter feature is consistent with the differences in the heating distributions (cf. Figs. 1 and 10). Plots of the fields for the wave-CISK and Mak schemes (not shown) exhibit the same general features and differ along lines consistent with the differences of the total heating distributions displayed in Fig. 10. Specifically, there is an increase in the magnitude and a decrease in the horizontal scale of the vertical velocity for both schemes.

6. Conclusion

Analytic solutions for nonlinear diabatic quasi-geostrophic surface frontogenesis have been presented. Results for prescribed heating document the basic thermal and dynamical response of the geostrophic flow and the associated ageostrophic motion to the forcing in the presence of a stretching deformation field. It is shown that only surface heating can directly alter the surface temperature field; interior heating can have an indirect effect by the induced ageostrophic surface convergence. In the case of condensational heating, the results support the findings of Williams *et al.* (1981). Such heating greatly intensifies the frontogenesis aloft and strengthens the cross-frontal circulation. In addition, the heating increases the static stability near cloud base and decreases it near cloud top. The amplification of the rising motion is

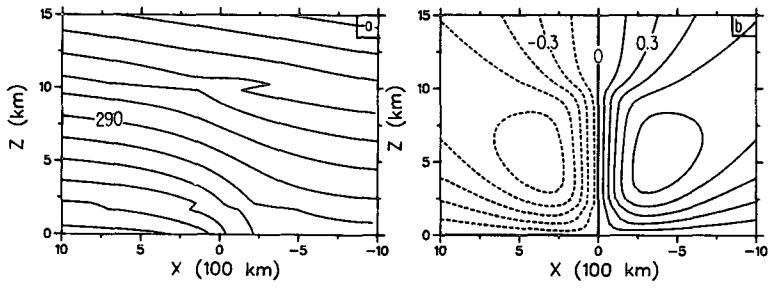

FIG. 11. The dimensional potential temperature (a) and the vertical velocity (b) at $\alpha t = 2$ for a front with the intermediate CISK parameterization. C.I. is 5 K in (a) and 0.15 in (b). Compare with the adiabatic and prescribed heating cases in Fig. 6.

qualitatively consistent with observations (cf., for example, Sanders, 1955, and Ogura and Portis, 1982) though the strong prefrontal subsidence noted by the latter reference is not predicted here.

It should be noted that the strengthened vertical motion, which is thermally direct (for warm sector precipitation) and hence frontolytic, is insufficient to negate the frontogenetic nature of the heating. This finding agrees with Thorpe (1984). The horizontal component of the cross-frontal circulation consists of frontogenetic low-level and frontolytic high-level branches. Quasi-geostrophic theory predicts the structure of this component but does not allow for its feedback on the thermal field.

Solutions with different CISK cumulus parameterizations all predict a concentration of the heating and rising motion near the surface front in the warm sector. Wave-CISK solutions predict slightly narrower heating which is more than three times stronger than solutions with a scheme due to Mak (1982). An intermediate scheme results in maximum heating roughly half that of wave-CISK. In these cases the effective large-scale static stability is not allowed to become nonnegative (the nondimensional heating parameter Δ equals unity). The convergent and finite solutions indicate that the growth rates of any instabilities are finite for each of the three schemes. Series solutions with $\Delta > 2$ (not shown) are not convergent, suggesting infinite growth rates at some wavelengths.

Though the present results illuminate the physical processes active in diabatic frontogenesis, the model formulation has several limitations. The shortcomings of quasi-geostrophic frontal theory are well-known (e.g., Hoskins, 1982). A companion study (Mak and Bannon, 1984) employs a semigeostrophic approach to include advection by ageostrophic flow components. Further, the cumulus parameterization used here suffers from the need to specify the heating profile and the presence of "anti-clouds" in regions of large-scale subsidence. Such simplifications have been introduced for mathematical expediency.

Acknowledgments. Financial support in part was provided to PRB jointly by the National Science Foundation (NSF) and the National Oceanic and Atmospheric Administration under Grant ATM80-26790 whereas MM received financial support from NSF under Grant ATM-8311175. Discussions with Prof. Victor Barcilon on integral equations benefitted PRB. Joseph A. Zehnder kindly provided the FORTRAN program subroutine to perform the numerical quadrature.

APPENDIX A

Integral Equation Formulation with CISK Heating

In this Appendix it is shown that the series expansion solution (2.8) to the diabatic problem with a CISK parameterization is equivalent to a Neumann series solution to the associated integral equation formulation. The substitution of (5.1), (5.4), (2.4a) and (2.1) into (2.2) yields

$$\frac{d}{dt}\left[\left(\frac{\partial^2\phi}{\partial x^2}+\frac{1}{S}\frac{\partial^2\phi}{\partial z^2}\right)+\Delta\left.\frac{\partial\phi}{\partial z}\right|_{z_B}\frac{dG}{dz}\right]=0. \quad \text{(A1)}$$

The initial condition is $\partial\phi/\partial z = \theta_0(x)$ at $t = 0$, and the lower boundary condition is $\partial\phi/\partial z = \theta_0[x\exp(\alpha t)]$ at $z = 0$. Separating ϕ into adiabatic and diabatic components, as in (2.6) where ϕ_A satisfies (A1) with $\Delta = 0$ (see Bannon, 1983), and making use of the fact that the solution of

$$\frac{dq}{dt}=0 \quad \text{(A2)}$$

is

$$q(x, z, t) = q(xe^{\alpha t}, z, 0), \quad \text{(A3)}$$

we obtain the following equation for ϕ_D:

$$\frac{\partial^2\phi_D}{\partial x^2}+\frac{1}{S}\frac{\partial^2\phi_D}{\partial z^2}=\Delta\frac{dG}{dz}[\theta_0(xe^{\alpha t})-\theta(x, z_B, t)]. \quad \text{(A4)}$$

The Green's function for the operator on the left-hand side of (A4) which satisfies $\partial\phi_D/\partial z = 0$ at $z = 0$ is

$$\phi_G(x-x', z, z')=\frac{1}{4\pi}[\ln r_+ + \ln r_-], \quad \text{(A5)}$$

where $r = (x - x')^2 + S(z \pm z')^2$. Hence ϕ has a solution of the form

$$\phi=\phi_A+\Delta\int_{-\infty}^{+\infty}dx'[\theta_0(x'e^{\alpha t})-\theta(x', z_B, t)]\times\int_0^{\infty}dz'\phi_G\frac{dG(z')}{dz'}. \quad \text{(A6)}$$

Use of the heating distribution (5.3) makes the z' integral straightforward. Differentiation of the result with respect to z and evaluation at $z = z_B$ yields

$$\theta_B(x, t)=\theta_A(x, z_B, t)+\lambda\int_{-\infty}^{+\infty}dx'K(x-x')\times[\theta_B(x', t)-\theta_0(x'e^{\alpha t})], \quad \text{(A7)}$$

where $\theta_B(x, t) = \theta(x, z_B, t)$, $\lambda = -\Delta$ and

$$K(x-x')\equiv\frac{\partial}{\partial z}[\phi_G(x-x', z, z_B)-\phi_G(x-x', z, z_T)]|_{z=z_B}. \quad \text{(A8)}$$

Knowledge of θ_B enables the full field to be obtained using (A6). This integral equation is a modified Fredholm equation. It is singular in that both limits of integration are infinite and the kernal K is not finite everywhere. However the kernel is only weakly singular. Use of a Neumann series solution on (A7) yields a result consistent with the expansion (2.8). Such a solution is convergent for all $|\lambda|$ such that $|\lambda| < \lambda_L$ where λ_L is the smallest singular point (e.g., eigenvalue) of the kernal K. Determination of λ_L was

not performed here, rather convergence was tested *a posteriori*.

APPENDIX B

Evaluation of Triple Integral (5.6)

The triple integral in (5.6) can be simplified by introducing the stretched coordinates

$$(X, Z, T) \equiv (xe^{\alpha t}, z, t) \tag{B1}$$

Then $dxdzdt = \exp(-\alpha T)dXdZdT$ and the limits of integration are unchanged. More importantly, use of (B1) enables one to write

$$\frac{d\theta}{dt} = \frac{\partial\theta}{\partial t} - \alpha x\frac{\partial\theta}{\partial x} = \frac{\partial\theta}{\partial T}. \tag{B2}$$

Then (5.6) may be written

$$\theta_n(X, Z, T) = \frac{-1}{2\pi}\int_0^\infty dZ_0\frac{dG(Z_0)}{dZ_0}\int_{-\infty}^{+\infty} dX_0 \times\left(\frac{Z_+}{R_+}+\frac{Z_-}{R_-}\right)\int_0^T dT_0\frac{\partial\theta_{n-1}}{\partial T_0}(X_0, Z_B, T_0), \tag{B3}$$

where the expression (3.13) for θ_I has been introduced. Inspection of (B3) indicates that the integral over T_0 is trivial. Hence

$$\theta_n = \frac{-1}{2\pi}\int_0^\infty dZ_0\frac{dG(Z_0)}{dZ_0}\int_{-\infty}^{+\infty} dX_0\left(\frac{Z_+}{R_+}+\frac{Z_-}{R_-}\right)\theta_{n-1}\Big|_0^T, \tag{B4}$$

where

$$\theta_{n-1}(X_0, Z_B, T_0)\Big|_0^T = \theta_{n-1}(X_0, Z_B, T) - \theta_{n-1}(X_0, Z_B, 0). \tag{B5}$$

Substitution of (5.7) into (B4) to evaluate θ_1 yields integrals over X_0 of the form

$$I \equiv \int_{-\infty}^{+\infty} dX_0\frac{1}{R_\pm}\tan^{-1}\left(\frac{X_0}{\xi}\right), \quad \xi > 0, \tag{B6}$$

which can be evaluated using the convolution theorem of the Fourier transform. One finds

$$I = \frac{\pi}{|Z_\pm|}\tan^{-1}\left(\frac{X}{\xi+|Z_\pm|}\right). \tag{B7}$$

Then θ_1 has the form

$$\theta_1 = \frac{(1-\bar{e}^{2\alpha t})}{\pi}\int_0^\infty dZ_0\frac{dG(Z_0)}{dZ_0}\left\{+\mathrm{sgn}(Z_+)\times\left[\tan^{-1}\frac{X}{1+Z_B+|Z_+|}-\tan^{-1}\frac{X}{1+|Z_+|}\right] + \mathrm{sgn}(Z_-)\left[\tan^{-1}\frac{X}{1+Z_B+|Z_-|} - \tan^{-1}\frac{X}{1+|Z_-|}\right]\right\}. \tag{B8}$$

For G given by (5.3), the Z_0 integral is also straightforward and the result is given by (5.9). Higher order terms may be evaluated in a similar manner.

REFERENCES

Bannon, P. R., 1983: Quasi-geostrophic frontogenesis over topography. *J. Atmos. Sci.*, **40**, 2266–2277.

Charney, J. G., and A. Eliassen, 1964: On the growth of the hurricane depression. *J. Atmos. Sci.*, **21**, 68–75.

Davies, H. C., 1979: Phase-lagged wave-CISK. *Quart. J. Roy. Meteor. Soc.*, **105**, 325–353.

Eliassen, A., 1959: On the formation of fronts in the atmosphere. *The Atmosphere and the Sea in Motion*, Rockefeller Institute Press and Oxford University Press, 277–287.

Emanuel, K. A., 1982: Inertial instability and mesoscale convective systems. Part II. Symmetric CISK in a baroclinic flow. *J. Atmos. Sci.*, **39**, 1080–1097.

Faller, A. J., 1956: A demonstration of fronts and frontal waves in atmospheric models. *J. Meteor.*, **13**, 1–4.

Fujita, T., 1959: Precipitation and cold air production in mesoscale thunderstorm systems. *J. Meteor.*, **16**, 454–466.

Fultz, D., 1952: On the possibility of experimental models of the polarfront wave. *J. Meteor.*, **9**, 379–384.

Hayashi, Y., 1970: A theory of large-scale equatorial waves generated by condensation heat and accelerating zonal wind. *J. Meteor. Soc. Japan*, **48**, 140–160.

Hoskins, B. J., 1974: Mathematical models of frontogenesis II. *Colloquium on Subsynoptic Extratropical Weather Systems*, M. Shapiro, Coord., 616–639. [Available from NCAR.]

——, 1982: The mathematical theory of frontogenesis. *Annual Reviews in Fluid Mechanics*, Vol. xiv Annual Review, 131–151.

——, and F. P. Bretherton, 1972: Atmospheric frontogenesis models: Mathematical formulation and solution. *J. Atmos. Sci.*, **29**, 11–37.

Kuo, H.-L., 1974: Further studies of the influence of cumulus convection on large-scale flow. *J. Atmos. Sci.*, **31**, 1232–1240.

Lindzen, R. S., 1974: Wave-CISK in the tropics. *J. Atmos. Sci.*, **31**, 156–179.

Mak, M., 1982: On moist quasi-geostrophic baroclinic instability. *J. Atmos. Sci.*, **39**, 2028–2037.

——, 1983: On moist quasi-geostrophic barotropic instability. *J. Atmos. Sci.*, **40**, 2349–2367.

——, and P. R. Bannon, 1984: Frontogenesis in a moist semigeostrophic model. Submitted to *J. Atmos. Sci.*

Ogura, Y., and D. Portis, 1982: Structure of the cold front observed in SESAME-AVE III and its comparison with the Hoskins-Bretherton frontogenesis model. *J. Atmos. Sci.*, **39**, 2773–2792.

Ooyama, K., 1964: A dynamical model for the study of tropical cyclone development. *Geofis. Int. (Mexico)*, **4**, 187–198.

Pedlosky, J., 1979: *Geophysical Fluid Dynamics*. Springer-Verlag, 624 pp.

Raymond, D. J., 1975: A model for predicting the movement of continuously propagating convective storms. *J. Atmos. Sci.*, **32**, 1308–1317.

——, 1976: Wave-CISK and convective mesosystems. *J. Atmos. Sci.*, **33**, 2392–2398.

——, 1983: Wave-CISK in mass flux form. *J. Atmos. Sci.*, **40**, 2561–2572.

Roden, G. I., 1975: On North Pacific temperature, salinity, sound velocity, and density fronts and their relation to the wind and energy field. *J. Phys. Oceanogr.*, **5**, 557–571.

Ross, B. B., and I. Orlanski, 1978: The circulation associated with a cold front. Part II. Moist Case. *J. Atmos. Sci.*, **35**, 445–465.

Sanders, F., 1955: An investigation of the structure and dynamics of an intense surface frontal zone. *J. Meteor.*, **12**, 542–552.

Sawyer, J. S., 1956: The vertical circulation at meteorological fronts and its relation to frontogenesis. *Proc. Roy. Soc. London*, **A234**, 346–362.

Thorpe, A. J., 1984: Convective parameterization in a quasi-geostrophic diagnostic model of fronts. *J. Atmos. Sci.*, **41**, 691–694.

Williams, R. T., L. C. Chou and C. J. Cornelius, 1981: Effects of condensation and surface motion on the structure of steady-state fronts. *J. Atmos. Sci.*, **38**, 2365–2376.